ornl

**OAK RIDGE
NATIONAL
LABORATORY**

MARTIN MARIETTA

Helium Transport and Exhaust in Tokamaks: A Report on the International Workshop on Helium Transport and Exhaust Experiments Held at Gatlinburg, Tennessee, United States of America, April 16–18, 1991

J. T. Hogan
D. L. Hillis

Fusion Energy Division

HELIUM TRANSPORT AND EXHAUST IN TOKAMAKS:
A REPORT ON THE INTERNATIONAL WORKSHOP ON HELIUM TRANSPORT AND EXHAUST EXPERIMENTS HELD AT GATLINBURG, TENNESSEE, UNITED STATES OF AMERICA, APRIL 16-18, 1991

J. T. Hogan
D. L. Hillis

Date Published: December 1991

MASTER

CONTENTS

ABSTRACT

A workshop on helium transport and exhaust in tokamaks was held in Gatlinburg, Tennessee, April 16–18, 1991. The chief purpose of the workshop was to foster discussion of plans for future experiments in the study of adequate helium removal from advanced fusion devices such as the International Thermonuclear Engineering Reactor (ITER). The areas covered at the workshop are outlined, and the results presented are discussed in detail.

1. INTRODUCTION

A workshop on problems of helium transport and exhaust in tokamaks, under the auspices of the International Energy Agency and sponsored by Oak Ridge National Laboratory (ORNL) and by Forschungszentrum KFA/Jülich, was held April 16–18, 1991, in Gatlinburg, Tennessee. Representatives from major tokamak laboratories attended, and 24 talks were given on the experimental status of helium transport and exhaust investigations, on modeling studies and reactor issues, and on plans for future studies.

The rate of helium ash accumulation has long been recognized to be a fundamentally important determinant of fusion reactor performance, and this view has been reinforced by studies carried out during the Conceptual Design Activity of the International Thermonuclear Experimental Reactor (ITER) project. At present, there is debate on whether to use the more pessimistic L-mode energy confinement scaling to determine the size of "next step" devices, such as ITER, because L-mode plasmas have adequate helium removal properties. On the other hand, improved energy confinement in H-mode plasmas is accompanied by improved particle confinement and hence (it is assumed, in the absence of a large experimental database) by increased helium accumulation. The view adopted by the ITER team, on the strength of some experimental evidence, is that a small degradation of energy confinement due to low-level magnetohydrodynamic-type (MHD-type) activity ["grassy" edge-localized modes (ELMs) and sawteeth] will be sufficient to guarantee adequate helium removal while retaining most of the H-mode enhancement in energy confinement. Further study of this question has been deemed a "high-priority" research and development (R&D) task by the ITER design team. The chief purpose of the workshop was to foster discussion of plans for future experiments in this area.

The charges to the workshop were given by D. L. Hillis (ORNL), the workshop chairman:
- Determine which helium transport and exhaust experiments are planned for the near term (next six months) and longer term (up to two years).
- Identify new issues relating to helium transport and exhaust.
- Determine the most pressing issues to be addressed in the next two years.

The subject areas covered in the workshop were
- the role of helium transport and removal for reactors, in general, and for specific next-step devices, such as ITER,
- the status of present experiments [the Joint European Torus (JET), JT-60, the Tokamak Fusion Test Reactor (TFTR), DIII-D, ASDEX, the Texas Experimental Tokamak (TEXT), and TEXTOR],
- the status of modeling,
- proposals for new helium removal concepts, and
- plans for future experiments.

2. ROLE OF HELIUM EXHAUST IN REACTORS

G. Wolf (KFA/Jülich) described the influence of helium ash accumulation on the attainment of burn conditions when realistic levels of other (nonhelium) impurities are present. Analysis of the limitations on allowable ash content in reactors shows that a 10% He concentration is reached after about 10 energy confinement times (τ_E), or in 30–50 s for ITER. Attainment of ignition conditions is determined by the value of the ratio τ_{He}^*/τ_E (here τ_{He}^* is the global helium confinement time in the core plasma, including recycled helium). Allowable values of τ_{He}^*/τ_E were found to lie in the range 9–12 if impurity concentrations of up to 2% of C, B, and/or Be are present. The Advanced Limiter Test–II (ALT-II) helium pumping experiments allow a direct experimental determination of the ratio τ_{He}^*/τ_E. The ALT-II experiment gives an acceptable value, τ_{He}^*/τ_E near 10, but this is obtained under L-mode confinement conditions. There are as yet no similar results from divertor tokamaks with active pumping.

More detailed analysis of the helium particle balance allows us to compare pump limiter and divertor helium exhaust. The helium accumulation is governed by the exhaust efficiency (ε) and by the repenetration efficiency (γ) (or boundary screening parameter) of helium which is not exhausted. The "first pass" of helium exhaust depends mostly on intrinsic core confinement (τ_{He}^1); after that, the pumping and boundary screening properties of limiter or divertor plasmas determine the helium confinement (τ_{He}^2). As an example, while the exhaust efficiency for the planned JET pumped divertor is low (~1%), the repenetration probability is even lower (~10^{-3} or 10^{-4}). This raises the question: which is more important, the low exhaust efficiency (common to pump limiters and divertors) or the even lower repenetration probability for divertors? It appears that a highly recycling divertor gives better shielding against repenetration.

Because there is only a narrow path to reach ignition between confinement that is "too good" (preventing exhaust) and "too bad" (preventing ignition), the following questions must be resolved:

- How large are the intrinsic "first-pass" confinement time τ_{He}^1 and the steady-state confinement time τ_{He}^2, and how do they depend on confinement regime?
- How large a fraction of the helium exhaust impinges on the pumped channel of the divertor; what is the loss of exhaust efficiency due to channels that are not pumped?
- What is the role of neutral helium which enters regions where high recycling conditions are not applicable? What is the role of profile wings on the divertor plate? (A large friction force is absent here.)
- What is the ratio of shielding (repenetration) to exhaust efficiency?
- How do ELMs change the conventional picture?

D. Post [Princeton Plasma Physics Laboaotory (PPPL) and ITER team] reviewed the ITER design and described helium exhaust issues. ITER is the first experiment to be considered by the fusion community for which helium exhaust is a determining problem: a burn duration of only 10–30 s can be expected (well short of the planned 200 s) if the helium content cannot be controlled. The overall ITER configuration is determined by constraints imposed by confinement scaling, beta limits, and the volt-seconds and space

requirements for the central solenoid (radial build) and by shielding and coil stress limits. The plasma current, safety factor, and aspect ratio are thus based on the international experimental community's L- and H-mode database, which predicts that $I_p = 22$ MA is required to attain ignition, with $\tau_E = 5.5$ s under ELM-free conditions. This confinement must be derated for the "ELM-y" conditions needed to prevent impurity accumulation.

Long-pulse H-modes with low-level ("grassy") ELM activity have been demonstrated on DIII-D and ASDEX. The view of the ITER team is that one can thus rely on "ELM-y" H-modes so as not to exceed a 10% He ash concentration in steady state. The technique of avoiding central helium accumulation with "ELM-y" H-modes and sawtooth control is made plausible by providing active measures for current profile control, using current drive schemes. It is expected that the current drive system can keep the sawtooth inversion radius ratio $r_s/a \sim 0.2$–0.3, and there is not a large confinement deterioration if $r_s/a < 0.5$. Study of the impact of helium content on the plasma current required to meet ignition conditions shows that ~1 MA of additional plasma current would be needed for each additional percentage point of helium concentration present in steady state. Attainment of acceptable helium concentrations ($n_{He}/n_e \sim 10\%$) requires $\tau_{He}^*/\tau_E < 10$ to reach Q = 5–10. Encouragingly, $\tau_{He}/\tau_E \sim 1$–3 is found for L-mode conditions in TEXTOR, TFTR, and JT-60 [where τ_{He} is related to the global helium confinement time τ_{He}^* by the relation $\tau_{He}^* = \tau_{He}/(1 - R_{He})$ and R_{He} is the helium recycling coefficient].

In addition to the core physics considerations, the fact that ITER produces a flux of ~4×10^{20} He atoms/s that must be pumped presents tasks for edge physics and engineering. Most of the helium flux entering the scrape-off layer (~90%) must be pumped, but this is not true for the flux hitting the plate. The helium flux at the plate is 10^{25} atoms/s, while the flux at the pump is 10^{22} atoms/s. Approximately 4×10^{20} He atoms/s must be pumped, that is, less than 1% of the plate flux. This high divertor recycling condition is possible only with a divertor plasma which is many mean free paths thick. The ITER divertor has a double-null configuration. Of the 200 MW of alpha power produced in ITER, 100 MW is radiated and 100 MW flows into the scrape-off layer. Flux surface expansion in the divertor channel and tilting of the divertor plates leads to a 16-fold reduction in the heat load at the divertor plate. Plasma conditions of $T_e \sim 5$–10 eV and $n_e \sim 5 \times 10^{14}$ cm^{-3} are expected at the plate, on the basis of predictions of validated two-dimensional (2-D) models. Extensive recycling is predicted (the divertor plasma is expected to be many ionization mean free paths thick) so that particles will be recycled 100–1000 times. The helium flux at the divertor plate is thus 1000 times greater than the helium flux which enters the scrape-off layer. This flux amplification allows helium pumping to be efficient. The ITER design provides for 700 m^3/s of helium pumping facing the plasma and 1500 m^3/s at the pump end. In addition to this problem of helium exhaust, high peak loads on the divertor plate, disruption forces, and compatibility of the divertor with proposed heating and current drive schemes are also important topics.

Helium transport and exhaust is a high-priority R&D issue for ITER. Some specific issues that should be addressed:

- Characterize helium confinement in the various regions of interest:
  - in the core plasma,
  - along field lines in the scrape-off layer,
  - in the pumping ducts.
- Understand D/T and He isotope spatial separation on the divertor plate.
- Perform "ELM-y" H-mode experiments to validate the ITER strategy.

3. STATUS OF HELIUM TRANSPORT AND REMOVAL EXPERIMENTS

3.1 JET

M. von Hellerman (JET) described the status of JET investigations of helium transport and removal. The conditions expected for full performance in JET have led to a requirement to make reliable absolute measurements of the alpha particle density. With 40 MW of heating power, ~5 MW of alpha power is expected, representing a 2- to 3-A current of helium. It is important that measurements be made with a known absolute source. The JET experiments employ helium fueling and deuterium diagnostic beams, so that central alpha fueling can be simulated. Present JET helium beams can inject 7 A of helium current and thus have a capability that is ~3–5 times larger than the expected JET alpha current. The status of the diagnostic capability on JET and results of helium transport were discussed.

3.1.1 Diagnostic Considerations

Diagnostic codes and techniques have improved over a five-year period to the point where the helium density measurements can now be made with charge-exchange recombination spectroscopy (CXRS) to within the required 25% uncertainty. Spatial profiles of helium density have been obtained for the plasma core ($r/a < 0.5$) in L- and H-mode plasmas. An extensive database of helium atomic physics rates has been established; a database for the energy range from 1 to 500 keV is available, and apparent discrepancies of a factor of 2–3 in the relevant rates have been resolved. Rate coefficients are found to be sensitive to the plasma environment, and the cross sections vary over the plasma spatial profile.

The accuracy of the measurement has been checked in a reference helium discharge by comparison with the LIDAR measurement of n_e. The helium profile is found to be nearly flat, with 45% He and 1.5% Be (relative to n_e). The radial n_e profile must be measured precisely since an uncertainty in n_e of ~10% corresponds to ~30% uncertainty in the helium density. The helium density was deduced to be in the range 55–25% (upper–lower bound) of n_e due to the 10% uncertainty in n_e.

The experimental difficulties in making alpha density measurements are related to the overlap of Be IV spectral lines with He lines and the question of the "plume." The Be line overlap problem requires beam modulation experiments to determine the Be charge-exchange component. The resulting spectrum then contains the edge recycling, core, and neutral beam ion components which can be discriminated. The "plume" effect is caused

by He^+ propagating along the magnetic field, excited by electron impact, thus leading to the pollution of the spectrum. On JET this effect can be reduced because of the ability to change the beam injection pitch angle, and the "plume to prompt" ratio can be reduced to ~20%. For parallel injection conditions, the plume should be a factor of five larger. Precise accounting for the beam divergence is needed owing to the smearing effect from several fans. This may yield a resolution of differences in interpretation of the "plume" magnitude on TFTR and JET. Since measurements of helium spatial gradients and fluxes depend on this, it would be hopeless to derive transport coefficient values from a plume-dominated discharge.

3.1.2 Active Fueling Experiments

He^4 beam (L-mode)

A sawtoothing L-mode discharge (22977) has been studied. The core helium density decays after the helium neutral beam is switched off. The edge recycle signal (He II at the edge) increases as the central helium density decays, so that the center and edge behave in opposite ways. A steady-state helium concentration of 10^{18} m^{-3} is found, corresponding to the amount injected into the plasma. The behavior of the central helium density is reasonably well modeled with *no inward helium pinch* and a helium diffusivity $D_{He} \sim 0.4$ m^2/s. This diffusivity is probably an overestimate, because sawtooth activity is present and such activity should be responsible for at least some of the outward helium transport. (Note: the L-mode helium transport database in JET is sparse because the combination of the helium fueling beam and the hydrogen diagnostic beam usually yields enough power to cause transition to the H-mode.)

He^4 and diagnostic (H) beams (H-mode)

In a sawtoothing H-mode discharge (23198), the central helium density does not decay, in contrast with L-mode, but levels out. As this happens, the H-mode decays. The measured helium spatial profile is flat to hollow. (A hollow helium profile is observed after the sawtooth crash.) The helium profile is no longer dominated by the central source, but by recycling at the edge. Analysis of helium profiles before and after the start of helium neutral beam injection (NBI) might separate the effects of the recycling and central sources. Comparison of the integrated helium beam source profile with observed helium profiles indicates strong expulsion from the q = 1 region. A diffusion coefficient $D_{He} \sim 0.5$ m^2/s is estimated for the H-mode discharge.

ICH He^3 minority

When ion cyclotron heating (ICH) is used with optimized coupling for a He^3 minority, a peaking factor of 1.7 in the central helium density is seen. The profile is more peaked than for NBI, and helium accumulates on axis.

L-mode and H-mode summary

A clear decay of helium density is seen for L-mode, occurring on a 0.5-s time scale. The injected helium can be accounted for, without evidence of pumping on carbon tiles. In H-mode, the helium profile is slightly peaked. The total helium content of the plasma is larger than the number of injected helium particles. Neutral-beam-injected helium (centrally injected) is effectively removed from the core in both L-mode and H-mode.

3.2 JT-60

H. Nakamura (Japan Atomic Energy Research Institute, Naka) presented the results of the JT-60 studies. Also, the welcome news was reported that first operation of JT-60U has been accomplished.

Helium transport experiments in L-mode plasmas with helium NBI (30 keV) and with helium gas puffing have been carried out. The experiments have been conducted for 10-s discharges in a lower single-null divertor configuration, with I_p = 1–1.5 MA and P_{NB} = 3–17 MW. The plasma is bounded by graphite and carbon-carbon composite tiles, and evidence of helium influx from prior implantation (in previous discharges) is observed. Helium densities are measured with a CXRS system with 30 channels, allowing 5-cm spatial resolution. Experiments have been done in Ohmic plasmas (with helium gas puffing) and in NBI-heated discharges, both with helium gas fueling (short and long pulse) and NBI central helium fueling (long pulse).

3.2.1 OH Case

In the Ohmic heating (OH) case a 200-ms helium gas puff leads to a constant He II signal in the divertor region over a period of ~1 s. While H_2 neutral pressures in the divertor region increase with n_e, there is no clear dependence of the helium density in the divertor on n_e. (Note: n_e refers to line-averaged density.) The helium enrichment factor is observed to be less than unity ("de-enrichment") and to decrease with n_e (~ $n_e^{-1.5}$) similar to Doublet III results of about 10 years ago. (The helium concentration in the main plasma in these experiments is estimated by assuming that n_{He} ~ $\delta n_e/2$.) The ohmically heated plasma apparently does not produce a strong enough particle flux to localize the helium to the divertor region. The helium mean free path is larger than that of hydrogen, and both are larger than the divertor characteristic length.

3.2.2 NBI Case

Two kinds of neutral beam experiments were conducted: with helium gas fueling and with helium NBI fueling (the former with both short and long pulses.)

Helium gas fueling

In helium gas fueling experiments that employed a short helium puff before the start of NBI (~10 MW), a decay was observed in the divertor helium density during both the OH and NBI phases, with the decay rate increasing with the application of NBI (L-mode). Both He II and H_β signals in the divertor dropped during NBI. Short-pulse fueling during NBI produced the same behavior in He II, but the H_β signal increased slightly. Long-pulse helium puffing during NBI produced an increase in the divertor He II. The H_β signals did not increase. For NBI-heated discharges with helium gas puff, the hydrogen and helium neutral pressures scaled as $\sim n_e^2$ to n_e^3. This indicates that helium can be localized near the divertor in NBI heating cases. The helium enrichment factor η for long-pulse helium fueling is ~0.7–0.9, while for short-pulse fueling $\eta \sim 0.3$–0.6. Specifically, the helium fueling efficiency for short-pulse helium gas injection with $P_{NB} = 10$ MW and $n_e \sim (2$–$4) \times 10^{13}$ cm^{-3} was $\eta \sim 1.0$, and for long-pulse fueling with $P_{NB} = 15$ MW and $n_e \sim (3$–$6) \times 10^{13}$ cm^{-3} it was $\eta \sim 0.4$–0.5.

Helium NBI fueling

Helium neutral beam fueling experiments were conducted with helium NBI (0.4 MW at 30 keV with 2-s pulse) added to hydrogen NBI (10 MW at 65–70 keV with 3-s pulse). The He II signal in the divertor was observed to increase continuously while the helium NBI was firing, then leveled off. Centrally peaked helium spatial profiles were observed. These can be modeled with an inward pinch which is slightly larger than that for the bulk plasma, with coefficient $C_v \sim 1$–1.5. The inward pinch is parametrized as $V_{inward} = -2C_v D_{anomalous} r/a^2$, with $D_{anomalous} \sim 0.4$ m^2/s.

The metastable content of the helium neutral beam was of concern for these experiments, and it was found that the fraction of metastable helium was <1%. The shine-through of the helium neutral beam (30 keV) is greater than that of the hydrogen neutral beam (40 keV), 20% vs 5% at $n_e \sim 4 \times 10^{13}$ cm^{-3}. For NBI-heated discharges with helium NBI, both the hydrogen and helium neutral pressures scaled as $\sim n_e^3$ and the helium enrichment factor was found to be lower for helium NBI than for helium gas puffing (~0.3 with helium NBI and ~1.0 for helium gas fueling, both at $n_e \sim 4 \times 10^{13}$ cm^{-3}). In an L-mode fusion reactor the thermalized alpha particles can be readily exhausted with a pumping speed of some tens of cubic meters per second.

3.3 TFTR

E. Synakowski (PPPL) presented the TFTR results. Study of helium transport is being pursued on TFTR because it could provide valuable insights into the mechanisms underlying enhanced confinement regimes, such as the "supershot" mode, and offer clues as to their differences from L-mode confinement. In addition, solving the reactor ash problem requires knowing the ratio of particle confinement time τ_p to energy confinement time τ_E. To understand the basic mechanisms, looking at local transport relations and comparing these results for different species are advocated. Thus, important

questions to be addressed with helium transport experiments are: what are the local relations between bulk plasma and helium transport properties, and what is the role of convection in various confinement regimes?

On TFTR these questions have been explored with helium transport studies in 13- to 14-MW L-mode and supershot regimes with balanced NBI. Helium transport has been compared with that of other impurities (notably Fe). The plasma conditions for the experiments were as follows:

Case	$n_e(0)/\langle n_e \rangle$	$T_i(0)$ (keV)	$T_e(0)$ (keV)	Z_{eff}	B_T (T)	I_p (MA)	P_{NB} (MW)
L-mode	1.2	3.5	3.5	1.5	4.8	1.0	13
Supershot	2.1–2.4	20–25	6–8	3.0–3.5	4.8	1.0	13

The experiments have been analyzed both with the MIST code and by calculating the measured time histories of helium density and gradients to extract the diffusivity and pinch velocity directly. In the MIST analysis the local $n_{He}(r,t)$ is measured, along with the time history of the helium source from the bumper limiter. This technique has limitations since both the time-to-peak of the injected helium and the helium density decay are modeled, and it is difficult to model both correctly. This circumstance has stimulated efforts to use the measured local gradient and flux and integrate radially to get the total helium flux inside the source-free core region ($r/a < 0.67$ for TFTR). This provides an actual measurement of the helium diffusivity and inward pinch. Application of the direct method produces results similar to MIST analysis for some cases, while others disagree.

In supershots, the helium profile reaches a fixed, centrally peaked shape, which then decays in time, due to pumping by the well-conditioned wall. The L-mode helium spatial profile is much flatter. A larger helium diffusivity is found for L-mode conditions than for supershots, with $D_{He} \sim 1-3 \text{ m}^2/\text{s}$ for both cases over much of the cross section. The differences between supershot and L-mode helium diffusivities are found mostly in the center ($\rho/a < 0.35$), while the pinch velocity is similar in both cases, except possibly at the edge. In cases where power balance calculations can be made (supershots) it is found that $D_{He}(r) \sim 0.5-1.0 \chi_i(r)$.

Electron perturbative transport analysis for the same discharges shows that n_e transport is quite probably very different from that for steady-state coefficients and also differs markedly from the helium values. Helium is found to be transported to the center more rapidly than n_e after a gas puff. The helium and iron diffusivities are, on average, larger than the diffusivities for n_e found in perturbative experiments. It is found that to study helium transport coefficients it is necessary to look at helium; using results for electron transport coefficients (D_e or χ_e) can give a misleading impression.

A comprehensive drift wave toroidal model study is being undertaken. The drift wave toroidal analysis code developed by G. Rewoldt et al. (PPPL) is used to predict

ratios of transport coefficients given the measured background profiles. An anomalous inward pinch is predicted in some cases by η_i-type theories, and this justifies using a $D\nabla$ $n + n V_{pinch}$ form for the helium flux.

3.4 DIII-D

M. Ali Mahdavi (GA) presented a review of earlier Doublet III results on helium enrichment and of present DIII-D particle control experiments.

3.4.1 Review of Doublet III Results

Helium enrichment experiments were conducted with the expanded boundary divertor configuration in Doublet III. The helium enrichment factor was always found to be smaller than 1. In contrast to results for argon, the helium mean free path was much larger than the divertor plasma scale length (the argon mean free path was smaller). Thus, argon was found to be trapped in the divertor and easily ionized there. This divertor trapping was enhanced by hydrogen (thus n_e) buildup. A divertor shielding factor ~ 5×10^{-3} is desirable to minimize particle exhaust requirements. If it is larger than this, core fueling must be supplemented with a divertor gas puff, which reduces impurity content.

3.4.2 DIII-D Collaborative Advanced Divertor Program

A new divertor particle control program, the Advanced Divertor Program (ADP), is being carried out on DIII-D. Two groups of experiments are under way: creation of a baffled high-pressure region near the outer strike point by means of a toroidally symmetric ring, and studies of plasma confinement modification through bias of this ring structure. The bias voltage has produced up to 6 kA of current flowing in the scrape-off layer, with little evidence to date that this current penetrates beyond the separatrix. Bias-induced $\mathbf{E} \times \mathbf{B}$ shifts in the heat and particle deposition profiles are observed, and the radial electric field component produced by biasing can enhance the pressure under the baffle. The applied bias voltage has been observed to modify the H-mode power threshold. There is a minimum in the power threshold at +75 V, and up to a three-fold increase in the threshold is observed at +400 V. The effect on confinement is only 10% at high power with negative bias and there is some effect of bias on ELM activity, but this is not reproducible. The maximum baffle pressure without bias rises with P_{NB} and decreases sharply when the X-point is moved with respect to the optimum position. Negative bias raises the pressure to restore some of this loss. Thus, for ITER, it may be possible to enhance pumping using a bias system.

3.5 TEXT

W. Rowan (University of Texas–Austin) reviewed TEXT experiments on helium particle confinement. Because the functional dependence of (normalized) τ_p on

(normalized) density in TEXT is similar to that reported for JET, JT-60 and Alcator, it is suggested that transport in TEXT is similar to that in larger machines. Global particle confinement in helium plasmas is found to have a different scaling from hydrogen for $\langle n_e \rangle < 3 \times 10^{13}$ cm^{-3}, while $\tau_p{}^{He}$ is estimated to be twice as large as the hydrogen particle confinement time. Experiments on rotation effects on particle confinement are planned. It is expected that electrostatic turbulence will be found to be the main contributor to transport.

3.6 TEXTOR

3.6.1 ALT-II Program

R. Moyer (University of California–Los Angeles) outlined the main results obtained so far in the ALT-II particle control program on TEXTOR. Experiments with the ALT-II pumped limiter have established the characteristics of this system, which is used in helium transport and removal experiments. Hydrogen particle exhaust efficiencies of 5–10% have been achieved. However, wall effects such as pumping and gas release are still important. Plasma plugging at the pump limiter throats has been predicted by the EIRENE code (D. Reiter, KFA/Jülich) and observed in experiments. A nonlinear increase in pump pressure is observed, as a function of n_e, for $n_e > 4 \times 10^{13}$ cm^{-3}. A flux amplification factor ~ 1.5 is estimated.

3.6.2 Helium Transport and Removal Experiments

D. Hillis (ORNL) surveyed TEXTOR experiments on helium transport and removal. Previously described helium transport and removal experiments under L-mode conditions in TEXTOR show that helium (injected with gas puffing) is removed from the core within ~1 s, with an exhaust efficiency ~ 8%. This exhaust efficiency is similar to that for hydrogen in these experiments; no helium enrichment is observed.

Experiments with an externally applied bias have produced an enhanced confinement regime on TEXTOR. Because of probe heat flux limitations, this regime is restricted to low injected power levels (~200 kW). Characteristic "H-mode" behavior in the H_α signal is seen, and the plasma density rises while the H_α drops, indicating increased particle confinement. Measurements of the helium concentration show that the helium decay time is longer with the application of polarization bias. Without polarization, the helium increases continually during the discharge in the pumping duct (up to 0.02 mTorr). In discharges with polarization, the helium pressure begins to rise, but when the polarization bias is applied it drops by more than a factor of five. When NBI starts, H_α fluctuations begin; increases in helium pressure in the duct associated with these fluctuations are correlated with the observed bursts. The helium pressure in the duct seems consistent with the measured increase in core retention. In discharges without H_α fluctuations, the duct helium pressure is reduced at the onset of polarization and stays low throughout the discharge.

H. Euringer (KFA/Jülich) reported on recent upgrades to the TEXTOR neutral beam heating system to provide energetic helium beams for fueling the plasma center to simulate a helium ash concentration inside the plasma core. After conditioning, the TEXTOR beam injectors can provide up to 2.3 MW of ^{4}He beams at 50 kV and 45 A for several seconds. One day of operation is possible without regeneration of the cryopumps. The pumping of helium within the neutral beam line is achieved by careful preconditioning of the cryosurfaces with argon. The cryopumps within the beam line work without modification at a temperature of 4.2 K with a pumping speed for helium which is about 36% that of H_2. The optimum Ar:He ratio of the pumping layer on the cryopump is 30:1. First measurements of helium neutral beam fueling of the plasma core have just begun.

K. H. Finken (KFA/Jülich) reported on helium measurements performed in the pumping ducts of TEXTOR. Neutral helium measurements in the pumping duct are difficult with a residual gas analyzer (RGA) since D_2 and helium have the same mass; therefore, a specialized pressure measurement was developed to measure helium pressures in the pumping duct in the presence of a majority species of D_2. This measurement consists of an absolutely calibrated modified Penning gage that ionizes the helium atoms and produces a visible line at 587.5 nm from the 3d-2p transition of helium. It was found that the helium line intensity is nearly proportional to the partial pressure of helium over the pressure range of interest. The light emitted from the Penning discharge is collected by a lens, transferred via a fiber-optics bundle, and spectrally resolved by interference filters. The helium concentration measurement is found to be accurate to about 1% concentrations. Typical helium pressures for TEXTOR were found to be about 0.1 mTorr. By using this helium pressure measurement in the pumping duct of TEXTOR it was found that fueling efficiencies of about 100% for low-density plasmas and about 50% for high-density plasmas were obtained after gas puffing from the vessel wall. Helium can be implanted and stored in the walls and released in subsequent discharges. The required helium density at the wall is of the order of a few times 10^{12} atoms per square centimeter. The helium liberated from the walls can be ionized in the boundary layer of the plasma, leading to a shielding of the main plasma. These results show that the helium stored transiently in the walls and liberated later in the discharge can play a role in the accumulation of helium in the exhaust gas.

J. Winter (KFA/Jülich) summarized recent results from JET and TEXTOR on helium wall pumping and outgassing from carbon, boron, and beryllium walls. In the case of hydrogen, pumping of particles by the vessel walls (wall pumping) has been observed for metallic wall surfaces or those made of carbon, boron, or beryllium. Hydrogen wall pumping has been used successfully for density control in present-day tokamaks; however, the wall pumping phenomenon for helium has not been studied in great detail so far. The first measurements from TEXTOR and JET indicate that the retention of helium in carbon or the wall pumping by carbon is small. In both tokamaks an instantaneous release of helium is observed at the end of the plasma discharge. Carbon and boron walls exhibit the same behavior. Recent JET experiments with

beryllium walls show reproducible helium wall pumping throughout a plasma discharge. No saturation of the beryllium walls was observed throughout the discharge. The pumping of helium by the beryllium walls is interpreted in terms of co-deposition of helium and eroded beryllium metal. Clearly, the tokamak wall still plays an important role in helium recycling and exhaust.

4. STATUS OF HELIUM TRANSPORT AND REMOVAL MODELING

4.1 HELIUM ENRICHMENT

D. Reiter (KFA/Jülich) surveyed helium enrichment modeling, from the early INTOR studies to results for the present ITER design. In the first helium enrichment studies for INTOR by Seki et al., preferential helium removal (2–3 times more effective than hydrogen removal) was found. When the problem was revisited with DEGAS, with a more refined atomic and surface physics model, no helium enrichment was observed. The conclusion at the time was that perhaps the improved atomic and surface data in DEGAS led to the discrepancy. This topic has been re-examined with the EIRENE code. Both cases have been restudied and both results reproduced. The improved atomic and surface data were indeed found to play a role, but an important additional parameter was found to be the kinetic energy of particles when they are ionized. For helium this was 4.4 eV, while for hydrogen it was 80 eV. Through charge-exchange reactions, neutral hydrogen can recover energy lost due to wall interaction, while helium cannot. The code of Seki et al. followed reionized particles using a particle dynamics code, rather than coupling a fluid code to the neutral particle calculation. Thus, helium ions were preferentially collected by the sheath, while hydrogen ions escaped. The study described found enrichment or de-enrichment depending on whether the helium ions were kept or lost at the plate.

Helium accumulation in experiments or reactors depends on the probability of exhaust and of recycling back to the scrape-off layer and subsequent repenetration to the main plasma. For ITER, the pumping efficiency is calculated with the EIRENE neutrals code, while the B2 code describes plasma radial and parallel transport. Coupled EIRENE/B2 calculations indicate that a high recycling regime is possible for the ITER design.

4.2 HELIUM CONSIDERATIONS FOR ITER

D. Post (PPPL/ITER) presented the work of S. Cohen (PPPL/ITER) and co-workers pertaining to the ITER divertor and helium balance. Helium accumulation has been judged to be an important issue for ITER: a 5% reduction in helium content would reduce the required plasma current by 20%, increase the technology phase pulse length by 70%, and increase the divertor lifetime by 11%. ITER can obtain at most an 80-s ignition pulse without He exhaust. This is somewhat longer than previous estimates and results from the fact that if a strong pinch causes accumulation on axis and extinguishes the burn, then the outer radial regions of the plasma cross section will have a relatively

lower helium concentration and can still burn. Because the present ITER divertor design produces a large flux amplification factor, $A = 500-1000$, effectively all of the helium efflux is pumped, even though only a small fraction of the flux to the divertor plate is actually removed.

There is an important safety issue for ITER: a five-fold reduction in the tritium inventory would make the components "passively safe." Since half the releasable inventory is in the pumps, increasing the helium content in the exhaust stream could reduce the required tritium throughput. A number of options have been considered to enhance helium pumping and a factor of two improvement has been obtained through optimization. Two techniques to separate helium from D/T have been explored: super-permeable membranes and ICH to accelerate the helium pumping speed. An improved helium exhaust could significantly reduce the tritium inventory and increase divertor lifetime.

4.3 CORE HELIUM TRANSPORT IN ITER

M. Redi (PPPL) presented BALDUR code simulations of helium transport in ITER. These are carried out with a basic model scaled from JET H-mode results. The thermal diffusivities are $\chi_e(r) = \chi_e(0)(3 + 5r/a)$, with $\chi_e(r)/\chi_i(r) = 2$, the particle diffusivity $D = \chi_i/2$, and the pinch velocity $v_p = 0$. The helium recycle coefficient is taken to be $R_{He} = 0.95$, with boundary conditions $n_{He}(a) = 0.1n_e(a)$. The plasma is assumed to be ELM-free, while sawtooth effects are modeled using the Park-Monticello semi-empirical scaling for the period. The sawtooth inversion radius $r_s/a \sim 0.1$ for these calculations. A "soft" beta limit model, devised by J. Manickam, is used to enhance transport near maximum beta. Calculations have also been made using the helium pinch in L-mode suggested by experiments in TEXTOR, TFTR, and JT-60 and by results from TFTR supershot data.

Defining the inward helium pinch with the parameter C_v, so that $V = C_v D2a/r^2$, it is found that the alpha heating power drops very sharply for $C_v > 1$, while C_v as high as 2 quenches the ITER burn. Helium pumping in ITER has a large effect on ignition requirements: the ITER design produces ignition for $R_{He} \leq 0.5$ (but not for R_{He} as high as 0.95).

4.4 MODELING OF TEXTOR HELIUM TRANSPORT AND REMOVAL EXPERIMENTS

J. Hogan (ORNL) presented modeling results for the TEXTOR helium transport and removal experiments. Previously reported analysis of the TEXTOR experiments showed that a radially varying helium diffusivity $D_{He} \sim 1$ m^2/s, with an inward pinch with $C_v \sim 0.65-0.8$, was satisfactory to explain the observed decay. Here C_v is defined through

$$V = C_v(D_{He}/n_e)dn_e/dr .$$

Obtaining a good fit of radially resolved profiles required the assumption of a small (~10%) contribution of energetic (~50-eV) helium atoms recycled from the limiter.

Experiments on TEXTOR with a polarization limiter applying up to 900 V bias have shown evidence of improved particle confinement. Further analysis of these results, with the MIST impurity transport model, has revealed that with diffusivities approximately the same as for L-mode conditions the value of C_v required to fit the data is significantly increased. For these cases, $C_v \sim 1.4$–1.6, compared with $C_v \sim 0.65$–0.8 for similar discharges without polarization. This increase is approximately consistent with the increase in hydrogen particle confinement time, as estimated from DEGAS simulation of the fraction of light from recycling H which can be attributed to core ionization.

4.5 HELIUM EXHAUST DUE TO SAWTOOTH EFFECTS

S. Hu (University of Illinois) described BALDUR code simulations of helium transport. The removal of reactor alphas by sawtooth and fishbone effects has been explored with the Redi/Cohen transport model, including a small anomalous pinch. Only a 3% decrease in the ratio n_{He}/n_e is found when the sawtooth effect is varied. These small changes are due to refueling at the edge; the sawtooth effects themselves lead mainly to a redistribution of the alpha density profile. This suggests that edge alpha transport enhancement would be attractive.

4.6 FEEDBACK CONTROL OF THE BURN INSTABILITY

V. Varadarajan (University of Illinois) discussed the control of fusion burning in-stabilities. The creation of a self-tuning control system for a partially known system like a tokamak presents a substantial challenge. In particular, the evolution of the alpha density profile has a large effect on controller algorithms. Results of the study show that deuterium fraction variation and impurity (Fe) seeding are desirable schemes for burn control, whereas auxiliary power control is not desirable.

5. NEW CONCEPTS FOR HELIUM REMOVAL

5.1 HELIUM SELF-PUMPING

J. Brooks (Argonne National Laboratory) reported on the helium self-pumping concept. This process removes helium in situ by trapping it in freshly deposited metal surface layers of a limiter or divertor. In a fusion reactor the trapping material used for the self-pumping would be added to the pumping surface at a rate of 3–5 times the alpha production rate. The self-pumping concept could, if successfully implemented, eliminate the need for much of the vacuum pumping system, reduce the tritium inventory, and possibly achieve better helium removal. Candidate trapping materials include nickel, iron, vanadium, and molybdenum. Recent experiments with atom implantation into evaporated nickel show high helium trapping fractions. The first actual test of the self-pumping concept on an operating tokamak is planned for TEXTOR beginning about

November 1991. This test will use the ALT-I limiter head and evaporated nickel surfaces and will permit further evaluation of the self-pumping concept.

5.2 ENHANCED HELIUM REMOVAL TECHNIQUE

C. Chang (Courant Institute, New York University) described new techniques by which helium can be preferentially removed from reactor plasmas using directional ICH. This creates a tail with a distorted alpha velocity distribution in the intermediate energy range. Lower-energy particles are removed, while higher-energy alphas move inward. The technique promotes loss of particles with energy < 1 MeV, thus retaining the bulk of alpha heating. It is estimated that 30 MW of ICH would be needed to remove 2×10^{20} He atoms/s created in ITER. The technique is active for "first-pass" alphas, slowing down from 3.5 MeV, rather than for recycling alphas from the divertor.

6. PLANS FOR FUTURE EXPERIMENTS

6.1 ASDEX-UPGRADE

U. Schumacher (IPP-Garching) outlined plans for future helium experiments in the newly commissioned ASDEX-Upgrade experiment. ASDEX-Upgrade will study a large number of helium-related questions, including

- measurement of fusion products to simulate fast alpha particle losses, interaction with MHD modes, and slowing-down processes,
- spectroscopic investigation of helium transport in the plasma bulk and near the boundary, and
- studies of helium flow and retention in the divertor region.

Study of the helium exhaust in pumping experiments is also planned.

In earlier ASDEX fusion product experiments, the relatively low plasma current (~0.4 MA) gave rise mostly to prompt losses. In ASDEX-Upgrade, with a plasma current of 1.6 MA, most charged fusion products will be confined, producing secondary products, such as

$$D + {}^3He \rightarrow {}^4He + p$$

and

$$D + T \rightarrow {}^4He + n$$
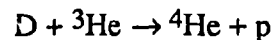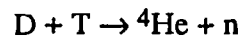
and thus it will be possible to study burnup.

Fast particle energetic tails can be produced with minority heating, but with restrictions to double-null divertor configurations with high I_p and at the lower limit of the available ICH frequency range.

Helium transport studies in the bulk and boundary plasma with CXRS will use both gas puff and 40-keV neutral beams. For studies of helium near the divertor plate, a swivel spectrometer with 5-mm spatial resolution will be used in combination with a spatially scanning divertor spectrometer. With a location just in front of the divertor

plate, this will enable a tomographic study of the helium distribution as a function of distance from the plate.

6.2 TEXTOR (CXRS)

H. Euringer (KFA/Jülich) reported on an upgrade to the charge-exchange excitation measurements of the He^{2+} density in the plasma core using the neutral beams of TEXTOR. To more accurately determine the transport parameters (D_A, the anomalous diffusivity, and C_v) detailed radial profile measurements are necessary. The new CXRS system would provide ion temperature measurements and helium concentrations at about 15 radial positio;   ng the plasma minor radius. These new spatial helium concentration measurements will be available about January 1992.

6.3 DIII-D CAPABILITIES FOR HELIUM EXPERIMENTS

P. West (GA) gave an overview of the diagnostic capability of the DIII-D collaborative ADP. The DIII-D device at present has a 32-channel charge-exchange spectroscopy system, with 16 channels localized in the outer 4.5 cm and 250-μs time resolution, ASDEX fast gages for boundary neutral pressure measurements, multichord boundary spectroscopy, and helium neutral beam and gas puffing capability. A fast scanning probe is being installed at the outer midplane and an array of Langmuir probes is in place on the divertor tiles. Multi-pulse Thomson scattering (25-ms resolution) can resolve up to five spatial points in the scrape-off layer. There are long-range plans to carry out helium exhaust experiments as part of the ADP program.

6.4 HELIUM PUMPING WITH ARGON FROST TECHNIQUES

M. Menon (ORNL) described a possible technique for implementing active helium pumping in DIII-D. With argon frost applied to the cryopumping system in the Advanced Divertor baffle region, exhaust of 1–5 Torr•L/s of helium can be attained. By using one of the four DIII-D neutral beam lines, a comparable rate of energetic helium injection could be attained. However, D_2 absorption reduces the pump speed of the argon frost system and is a potential problem. This can be alleviated with a "squirt tube" design, in which the cryopump can act as a compound cryopump.

6.5 DETECTION OF ESCAPING ALPHA PARTICLES

R. Langley (ORNL) presented a technique that allows measurement of the pitch angle and energy distribution of escaped alphas as a function of time. The alphas are trapped in a set of layered foils, which are subsequently removed, melted and vaporized to remove the implanted helium. Quantitative mass spectrometry is then used to assess the helium level. Energy resolution of 70 keV is estimated. This method is not affected by plasma background, while other methods are affected by other forms of radiation.

7. DISCUSSION OF NEW ISSUES RAISED AT THE WORKSHOP

Several new issues were raised during discussions and were taken up at greater length. The first relates to the "plume" effect, which is important in the interpretation of CXRS measurements. As first described by R. Fonck in 1984, this effect can cause excited ions to contribute to the radial profile from regions far from the originally assumed beam-plasma interaction zone. In large, hot plasmas, e.g. in TFTR and JET, the plasma ion temperature can approach that of lower energy neutral beam components and make interpretation difficult. In addition, while the ratio of "plume to prompt" contributions to the charge-exchange signal is ~10% for oxygen, it can be as large as ~30–40% for helium. The magnitude of the effect depends on the reliability of the atomic data used and on proper modeling of the specific beam source geometry. When these are accounted for, accurate results are obtained. The discussion on this topic was led by E. Synakowksi (PPPL).

A modeling topic of importance to helium transport (and other questions) was discussed by D. Reiter (KFA/Jülich). While coupled calculations with multidimensional neutral and scrape-off layer transport have been reported for ten years, the existing techniques are so computationally demanding as to strongly reduce their usefulness. An "implicit coupling" technique has been developed which makes these kinds of calculations feasible for the first time. The conventional coupling in codes results in a "freezing" of the neutrals in the plasma calculation, and this drives the solution away from the desired high recycling solution. Also, fluctuations from the neutrals Monte Carlo solution drive the iteration away from the true solution. The implicit coupling technique incorporates memory of the past iteration history. By employing the same grid for neutrals and parallel transport, the noise generation (and subsequent inefficiency incurred by the necessity to track this noise through the scrape-off layer plasma) can be strongly reduced.

There was also discussion of the desirability of establishing a helium transport database, along the lines of the ITER H-mode database. This is, at least in principle, more feasible than a particle confinement database for hydrogenic transport, because the helium source is easier to characterize. However, from the workshop it is apparent that the helium database is relatively small at present, although a large expansion of experimental activity is planned in this area. Thus, this topic will be reconsidered at the 10th Plasma Surface Interactions Conference, to be held in Monterey, California, in the spring of 1992.

8. SUMMARY OF CAPABILITIES AND PLANS FOR HELIUM TRANSPORT AND EXHAUST EXPERIMENTS

The workshop participants constructed summary tables for diagnostic capabilities (for both core and scrape-off layer plasmas), of capabilities for helium input and exhaust, and a survey of experimental issues that they plan to address, in both the near term (up to

fall 1991) and the long term (up to spring 1993). Table 1 lists the core diagnostics for helium work that are available now or will be available in the near term, and Table 2 is a similar list of diagnostics for the scrape-off layer plasma in devices other than JET. Because of the extensive capabilities of JET in this area, the JET scrape-off layer and divertor region diagnostics are described separately in Tables 3a and 3b. The capabilities for helium injection and exhaust experiments are summarized in Table 4. Finally, Table 5 presents the issues that will be addressed in the near term and during the next two years.

Table 5 can thus stand as an expression of the answer to the final charge to the workshop: these topics are viewed as the most pressing issues to be addressed experimentally in the next two years.

Table 1. Core diagnostics

Machine	Type	Parameter	Resolution	Date available
JET	CXRS	$n_\alpha(r,t)$, $T_\alpha(r,t)$, $v(r,t)$, $F(v,r,t)$	—	Now
	NPA	$F(\varepsilon)$, $F(\varepsilon,r,t)$ Species mix	—	Now
JT-60 U	CXRS	$n_\alpha(r,t)$	30 points ($\delta r \sim 7$ cm)	June–July 1991
	160-keV He beam probe	$n_\alpha(r,t)$	20 cm (center)	
	Interferometer	n_e ($\sim 2n_\alpha$)	2 chords	Now
	Thomson scattering		[20–30 channels]	August 1991
TFTR	CXRS	$n_\alpha(r,t)$	10-cm spatial (outer half)	Now
			7-cm spatial	September 1991
	Fast-alpha CER	$n_\alpha(r,t)$		DT operation phase
	Gyrotron scattering			DT operation phase
	Impurity pellet			DT operation phase
TEXT	CXRS	$n_\alpha(r,t)$	$\delta r \sim 2$ cm	Now
ASDEX-U	SPRED	Z_{eff}	None	Now
	CXRS	$n_\alpha(r,t)$	11 (or 22) channels	December 1992 (NB)
	14.7 MeV	$n_{3_{He}}(r,t)$, $p + (D-^3He)$	To be determined	Plans
DIII-D	CXRS	$n_\alpha(r,t)$	32 channels (axis–separatrix)	Now
TEXTOR	CXRS	$n_\alpha(r,t)$	3 chords	Now
	CXRS		10 chords	October 1991
	Interferometer	n_e ($\sim 2n_\alpha$)		Now

Table 2. SOL/divertor diagnostics
(other than JET)

Machine	Diagnostic type	Parameter	Date available
JT-60 U	Edge Thomson scattering	n_e, T_e (separatrix)	August 1991
	Langmuir probe array	n_e, T_e (separatrix)	Now
	He II spectrometer	S_α	August 1991
	RGA	P_α	August 1991
	Penning or backscatter	P_α	(plan)
TFTR	Probes	n_e, T_e	Now
	UV/visible	E_α	Now
TEXT	Langmuir probes	n_e, T_e	Now
	Gridded probes	n_e, T_e	August 1991
	Spectroscopy		Now, August 1992 (divertor)
ASDEX-U	Boundary tomography spec trometer (using swivel mirror)	n_{HeI}, n_{HeII}	1992
	Divertor spectrometer	Flow velocities	January 1992
DIII-D	Scanning Langmuir probe	n_e, T_e (midplane)	Now
	Divertor Langmuir probe arrays	n_e, T_e (tile floor)	Now
	Divertor spectroscopy		Now
TEXTOR	Scanning Langmuir probe Second location	n_e, T_e	Now October 1991
	Thermal Li beam	$n_e(r,t)$	Now
	Thermal He beam	$T_e(r,t)$	Now
	He exhaust pressure	P_{He}	Now
	Laser ablation	n_e, T_e	Now
	He flux/spectroscopy	S_α	Now

Table 3a. Scrape-off layer diagnostics for JET
Information provided by M. A. von Hellerman

Parameter[a]	Available from/at position	Directly measured observable	Derived quantity	Spatial resolution	Spatial coverage	Repetition rate	Integration acquisition time	Available during campaign
n_{eb}, λ_n	Fast reciprocating Langmuir probe OCT 5D, top, R = 2.71 m, 10-cm vertical stroke	Probe characteristic	$n_e, \nabla_\perp n_e$		Single position, 6-cm sweep	3 × 200 ms excursions, 80 points maximum	5 ms (sweep)	90
	OCT 5D, top, R = 3.25 m, 25-cm vertical stroke	Probe characteristic	$n_e, \nabla_\perp n_e$		Single position, 25-cm sweep	3 × 200 ms excursions, 80 points maximum	5 ms (sweep)	91, PD
	Edge Thomson scattering OCT 5	Scattering spectrum	$n_e(r,z)$	1 × 5 cm	Midplane, 50 cm	0.5 Hz		91, PD
	Divertor Thomson scattering OCT 5	Scattering spectrum	$n_e(r,z)$	1 × 5 cm	Outer SOL, lower half	0.5–0.4 Hz	0.3 ns	91, PD
	KT1 VUV spectroscopy OCT 6 (horizontal/vertical)	Photon flux, selected lines	n_e(line ratios), $(\nabla n_e)_\parallel$	8–12 cm	Most of SOL, divertor	Every 100 ms		91, PD
T_{eb}, λ_T	Fast reciprocating Langmuir probe OCT 5D, top, R = 2.71 m, 10-cm vertical stroke	Probe characteristic	T_e profile, $(\nabla T)_\perp$		Single position, 6-cm sweep	3 × 200 ms excursions, 80 points maximum	5 ms (sweep)	90
	OCT 5D, top, R = 3.25 m, 25-cm vertical stroke	Probe characteristic	T_e profile, $(\nabla T)_\perp$		Single position, 25-cm sweep	3 × 200 ms excursions, 80 points maximum	5 ms (sweep)	91, PD
	Edge Thomson scattering OCT 5	Scattering spectrum	$T_e(r,z)$	1 × 5 cm	Midplane, 50 cm	0.5 Hz		91, PD
	Divertor Thomson scattering OCT 5	Scattering spectrum	$T_e(r,z)$	1 cm (transverse) × 5 cm (along beam)	Outer SOL, lower half	0.5–4 Hz	0.3 ns	PD
	KT1 VUV spectroscopy OCT 6 (horizontal/vertical)	Photon flux, selected lines	$(\nabla T_e)_\parallel$	8–12 cm	Most of SOL, divertor	Every 100 ms		91, PD

Table 3a. (continued)

Parameter[a]	Available from/at position	Directly measured observable	Derived quantity	Spatial resolution	Spatial coverage	Repetition rate	Integration acquisition time	Available during campaign
T_{ib}	KS5 visible D_α spectroscopy (ABAS) OCT 1, 7, midplane outer edge plasma	D_α spectrum	T_i, (∇T_i) min	$\int d\ell$ inside separatrix	OCT 1 to 7 midplane chord	Every 50 ms	20 to 50 ms	90, 91, PD
	OCT 8, extrapolate midplane bulk plasma		T_i (inside separatrix)	5–10 cm	OCT 1 to 7 midplane chord	Every 50 ms	20 to 50 ms	90, 91, PD
	KS7 visible poloidal edge spectroscopy OCT 4B, midplane outer edge plasma	D_α spectrum	$T_i(r)$	10 points with 1.5-cm resolution in SOL	Outer SOL 3.8–4.1 m	Every 1 to 3 ms	1 to 3 ms	91, PD
T_{zb}	KS4 visible charge-exchange spectroscopy OCT 8, top/bottom edge plasma, R = 3.1 m	Impurity spectrum	T_z, (∇T_z) min	$\int d\ell$	OCT 1 to 7 midplane chord	Every 50 ms	20 to 50 ms	90, 91, PD
	OCT 1, 7, midplane outer edge plasma		T_z, (∇T_z) min	$\int d\ell$	OCT 1 to 7 midplane chord	Every 50 ms	20 to 50 ms	90, 91, PD
	OCT 8, extrapolate midplane bulk plasma profile		T_z	5–10 cm	OCT 1 to 7 midplane chord	Every 50 ms	20 to 50 ms	90, 91, PD
	KS7 visible poloidal edge spectroscopy	Impurity spectrum	$T_z(r)$	10 points with 1.5-cm resolution in SOL	Outer SOL 3.8–4.1 m	Every 1 to 3 ms	1–3 ms	91, PD
P_{rad}	Bolometer KB1 OCT 2	$\int P_{rad} dl$	$P_{rad}(r,t)$	Of order 35 cm	Entire plasma	Every 50 ms	10 to 20 ms	90, 91, PD
	KS5 visible D_α spectroscopy (ABAS) OCT 1, 7, outer midplane edge plasma	D_α spectrum	Φ_o	$\int d\ell$	OCT 1 to 7 midplane chord	Every 50 ms	20 to 50 ms	90, 91, PD
	KS4 visible charge-exchange spectroscopy OCT 1, 7, midplane outer edge plasma	Impurity spectrum	Φ_z	$\int d\ell$	OCT 1 to 7 midplane chord	Every 50 ms	20 to 50 ms	90, 91, PD
	KT1 VUV diagnostics	Impurity spectrum	Φ_z	8–12 cm	Upper inner SOL	Every 100 ms	4–8 ms	90, 91, PD
n_{zb}	KS4 visible charge-exchange spectroscopy OCT 8, extrapolate midplane bulk plasma profile	Impurity CX spectrum	n_z, (n_d/n_e), Z_{eff}	5–10 cm	Midplane bulk plasma 3.1–4 m	Every 50 ms	20–50 ms	90, 91, PD
	KT1 VUV diagnostics	Impurity spectrum	$n_z(r,z)$	8–12 cm	Upper inner SOL	Every 100 ms	4–8 ms	90, 91, PD
	KT2 SPRED	Impurity spectrum	$n_z(r,z)$	5–20 cm	Midplane	Every 17 ms	17 ms	90, 91, PD

22

Table 3a. (continued)

Parameter[a]	Available from/at position	Directly measured observable	Derived quantity	Spatial resolution	Spatial coverage	Repetition rate	Integration acquisition time	Available during campaign
	KT4 XUV spectrometer	Impurity spectrum	$n_z(r,z)$	5–20 cm	Below midplane to outer strike zone	Every 17 ms	17 ms	90, 91, PD
$\int dn_{zvol} dV$	KS4 visible charge-exchange spectroscopy OCT 8, extrapolate midplane bulk plasma profile	Impurity CX spectrum	$\int d_z\, dv$	5–10 cm	Midplane bulk plasma 3.1–4 m	Every 50 ms	20 to 50 ms	90, 91, PD
R_{SOL}	Magnetic data evaluation codes IDENTC databank FAST, XLOC	Magnetic fluxes, fields	Equilibria flux surfaces		Entire torus			90, 91, PD
v_z	KS4 visible charge-exchange spectroscopy OCT8, extrapolate midplane bulk plasma profile	Impurity line shift	v_{tor} profile	5–10 cm	Midplane bulk plasma	Every 50 ms	20–50 ms	90, 91, PD
	KS7 visible poloidal edge spectroscopy OCT4B, midplane outer edge plasma	Impurity line shift	v_{pol} profile	10 points with 1.5-cm resolution in SOL	Outer SOL midplane	Every 1–3 ms	1–3 ms	91, PD
v_i	KS7 visible poloidal edge spectroscopy OCT4B, midplane outer edge plasma	D_α line shift	$v_{pol}(r)$	10 points with 1.5-cm resolution in SOL	Midplane outer SOL	Every 1–3 ms	1–3 ms	91, PD
I_{SOL}	Langmuir probes OCT 7 OCT 7B	Ion saturation current	I_{ion}		12 probes along upper target, 16 probes along lower target	Every 50 μs	5 ms	90, 91

[a]Notation used for key parameters:

n_{eb}	Midplane (boundary) separatrix electron density (primary input quantity to model determining divertor impurity retention)		n_{zvol}	Impurity content inside volume enclosed by LCFS
T_{eb}	Midplane separatrix electron temperature		R_{SOL}	Separatrix position in midplane
T_{ib}	Midplane separatrix deuteron temperature		v_i	Streaming velocity of ions along SOL
T_{zb}	Midplane separatrix impurity temperature		v_z	Streaming velocity of impurities along SOL
λ_n	Midplane scale length for density (perpendicular to separatrix)		I_{SOL}	Current in SOL
λ_T	Midplane scale length for temperature (perpendicular to separatrix)		Φ_0	Photon flux of neutral hydrogen line, $W/(cm^2 \cdot nm \cdot sr)$
n_{zb}	Midplane separatrix impurity density		Φ_z	Photon flux of impurity line, $W/(cm^2 \cdot nm \cdot sr)$
			Γ_g	Gas fueling influx

23

Table 3b. Divertor region diagnostics for JET
Information provided by M. A. von Hellerman

Parameter[a]	Available from/at position	Directly measured observable	Derived quantity	Spatial resolution	Spatial coverage	Repetition rate	Integration acquisition time	Available during campaign
n_{ed}	KS3$\frac{1}{2}$ fiberscope spectroscopy OCT 2, 3, 4, 5 divertor view	BeI lines spectrally resolved	$n_{ed}(r,t)$ (line ratios)	5 mm	Lower target area 0.5 × 13 cm	Every 50 ms	20–50 ms	PD
	KS3$\frac{1}{2}$ visible spectroscopy (roof lab link) OCT 1, lower target strike zone	BeI lines spectrally resolved	$n_{ed}(r,t)$ (line ratios)	10 mm	Lower target area 1 × 50 cm	Every 50 ms	20–50 ms	91, PD
	Target Langmuir probes OCT7 OCT 7B	Probe characteristic	$n_e(r,t)$	<1 cm	12 points on upper targets, 16 points on lower targets	Every 50 ms	5 ms	90, 91, PD
	Divertor Thomson scattering OCT5	Scattering spectrum	$T_e(r,z)$	1 cm × 5 ms	Inner divertor plasma	0.5–4 Hz	0.3 ns	PD
	X-point reflectometer	Microwave reflectometer vs frequency	n_e max along chord view lines		1 sight line			91
	Divertor reflectometer	Microwave reflectometer vs frequency	n_e max along chord view lines		2 sight lines			PD
	Microwave interferometer	Phase shift of microwave, z Frequency	$\int n_e dl$	Along chord; transverse 7 cm	2 sight lines			PD
n_{id}	From n_{ed} and n_{zd}							
T_{ed}	Target Langmuir probes OCT 8B	Probe characteristic	T_e	Point measurement, poloidal target plate	8 points on upper target, 16 points on lower target	Every 50 ms	5 ms	90, 91
	Divertor Thomson scattering OCT 5	Scattering spectrum	T_e	1 cm across beam × 5 cm (away beam)	Inner divertor plasma	0.5–4 Hz	0.3 ms	PD
	Edge Thomson scattering	Scattering spectrum	T_e	1 cm across beam × 5 cm (away beam)	50 cm midplane	0.5 Hz	0.3 ms	91, PD
	KT1 VUV spectroscopy OCT 6	Distribution of impurity ions	T_e	Sweeps SOL/ divertor	Inner upper SOL	Every 100 ms	4–8 ms	91, PD

24

Table 3b. (continued)

Parameter[a]	Available from/at position	Directly measured observable	Derived quantity	Spatial resolution	Spatial coverage	Repetition rate	Integration acquisition time	Available during campaign
T_{zd}	KT3½ visible spectroscopy (roof lab link) OCT 1, lower target strike zone	Impurity line shape	T_z	10 mm	Lower target 50 cm × 1 cm	Every 50 ms	20–50 ms	91, PD
	KS3½ fiberscope spectroscopy OCT 2, 3, 4, 5 divertor view	Impurity line shape	T_z	5 mm	Lower target 5 mm × 13 cm	Every 50 ms	20–50 ms	PD
	KT1 visible	Impurity line shape	T_z	Sweeps SOL/ divertor	Inner upper SOL	Every 100 ms	4–8 ms	91, PD
	KS3 vertical array OCT 1	Impurity line shape	T_z	28 cm	Single line of sight	Every 20 ms	20 ms	91, PD
	KS3½ toroidal view spectroscopy OCT 5B opposing views	Spectral line shape	T_z	∫dl in toroidal direction, Ø 12 cm of line of sight	Toroidal chord	Every 20–50 ms	20–50 ms	PD
T_{id}	KT3½ visible spectroscopy (roof lab link) OCT 1, lower target strike zone	Spectral line shape	T_i	10 mm	Lower target area of 1 × 50 cm	Every 50 ms	20–50 ms	91, PD
	KS3½ fiberscope spectroscopy OCT 2, 4, 5 divertor view	Spectral line shape	T_i	5 mm	Lower target area of 5 mm × 13 cm	Every 20–50 ms	20–50 ms	PD
	KS3½ toroidal view spectroscopy OCT 5B opposing views	Spectral line shape	T_i	∫dl in toroidal direction, Ø 12 cm of line sight	Toroidal chord	Every 20 ms	20 ms	PD
	KS3 vertical array OCT 1	Line shape	T_i	28 cm	Single line of sight	Every 20 ms	20 ms	91, PD
T_{targ}	CCD camera view	Plate emission, several filters	T_t (limited range) 2D	1 cm × 1 cm	1 poloidal set of target tiles	Every 20 ms	160 μs to 20 ms	90, 91, PP
	IR array	Plate emission, several filters	T_t (limited range) 2D	5 cm × 5 cm	1 poloidal set of target tiles			91, PP
p_0	Target pressure gages	Fast ionization gage	n^0_{di}, Γ^0_d in gage	5-mm hole	5 located in divertor targets 1 in lower X-pt tile			PD 91
v^0_d	KS3½ fiberscope spectroscopy OCT 2, 3, 4, 5 divertor view	Line shape D_α line	Γ^0_d (neutral influx), v_d	5 mm	Lower target area 0.5 × 13 cm	Every 50 ms	20–50 ms	PD
	KS3½ toroidal view spectroscopy OCT 5B opposing views	Line shape D_α line	v_{dll}	∫dℓ along toroidal chord	Toroidal chord Ø 12 cm	Every 20–50 ms	20–50 ms	PD

Table 3b. (continued)

Parameter[a]	Available from/at position	Directly measured observable	Derived quantity	Spatial resolution	Spatial coverage	Repetition rate	Integration acquisition time	Available during campaign
Γ_d^0	KT3$\frac{1}{2}$ visible spectroscopy (roof lab link) OCT 1, lower target strike zone	Line shape D_α line	Γ_d^0	10 mm	Lower target area 1 × 50 cm	Every 50 ms	20–50 ms	91, PD
	KT3$\frac{1}{2}$ fiberscope spectroscopy OCT 2, 3, 4, 5 divertor view	Line shape D_α line	Γ_d^0 (neutral influx), v_d	5 mm	Lower target area 0.5 × 13 cm	Every 50 ms	20–50 ms	PD
	KS3$\frac{1}{2}$ toroidal view spectroscopy OCT 5B opposing views	Line shape D_α line	v_{dll}	$\int d\ell$ along toroidal chord	Toroidal chord Ø 12 cm	Every 20–50 ms	20–50 ms	PD
v_{zd}	KT3$\frac{1}{2}$ fiberscope spectroscopy OCT 2, 3, 4, 5 divertor view	Impurity line shape	$v_{||}$	5 mm	Lower target area 0.5 × 13 cm	Every 50 ms	20 to 50 ms	PD
	KT3$\frac{1}{2}$ toroidal view spectroscopy OCT 5B opposing views	Impurity line shape	$v_{||}$	$\int d\ell$ toroidal chord Ø 12 cm	Toroidal chord Ø 12 cm	Every 20–50 ms	20 to 50 ms	PD
Γ_{zd}	KT3$\frac{1}{2}$ visible spectroscopy (roof lab link) OCT 1, lower target strike zone	Impurity line shape	Γ_{zd}	10 mm	Lower target area 1 × 50 cm	Every 50 ms	20–50 ms	91, PD
	KS3$\frac{1}{2}$ fiberscope spectroscopy OCT 2, 3, 4, 5 divertor view	Impurity line shape	$v_{||}$	5 mm	Lower target area 0.5 × 13 cm	Every 50 ms	20–50 ms	PD
	KS3$\frac{1}{2}$ toroidal view spectroscopy OCT 5B opposing views	Impurity line shape	$v_{||}$	$\int d\ell$ toroidal chord Ø 12 cm	Toroidal chord Ø 12 cm	Every 20–50 ms	20 to 50 ms	PD
Γ_z	Gas fueling	Reservoir pressure drop	Fueling rate	For each valve				90, 91, PD
P_{rad}	Bolometer data	$P_{rad, chord}$	$\int P_{rad} dV$, Abel inversion		Entire plasma, horizontal and vertical cameras			90, 91, PD
	KT3$\frac{1}{2}$ visible spectroscopy (roof lab link) OCT 1, lower target strike zone	Absolute photon flux	Φ_z	$\int d\ell$, 10 mm transverse	Lower target area 50 × 50 cm	Every 50 ms	20–50 ms	91, PD
	KS3 visible spectroscopy OCT 1	Absolute photon flux	Φ_z	$\int d\ell$, 12 mm transverse	Ø12 cm along chord	Every 20 ms	20 ms	90, 91, PD
	KS3$\frac{1}{2}$ fiberscope spectroscopy OCT 2, 3, 4, 5 divertor view	Absolute photon flux	Φ_z	$\int d\ell$, 5 mm transverse	Lower target area 13 × 13 cm	Every 50 ms	20–50 ms	PD
	KT1 (VUV/XUV) instrument	Absolute photon flux	Φ_z	8–12 cm	Full divertor (upper target)	Every 100 ms	4–8 ms	90, 91, PD

26

Parameter[a]	Available from/at position	Directly measured observable	Derived quantity	Spatial resolution	Spatial coverage	Repetition rate	Integration acquisition time	Available during campaign
R_{sp}	Magnetic data evaluation codes IDENTC databank FAST, XLOC		Configuration data in IDENTC		Average entire torus			90, 91 PD
	KT3$\frac{1}{2}$ visible spectroscopy (roof lab link) OCT 1, lower target strike zone	Line radiation distribution	R (max Φ)	10 mm	Lower target area 50 × 50 cm	Every 50 ms	20–50 ms	91, PD
	KL1 CCD cameras	Line radiation distribution	R (max Φ)	3 mm	40 cm Ø on target	Every 50 ms	160 μs to 2 ms	90, 91, PD
	KS3$\frac{1}{2}$ fiberscope spectroscopy OCT 2, 3, 4, 5 divertor view	Line radiation distribution on target	R (max Φ)	5 mm	Lower target area 13 × 13 cm	Every 50 ms	20–50 ms	PD
KT1	VUV diagnostic	Line radiation distribution on target	R (max Φ)	12 cm	Upper target	Every 100 ms	4–8 ms	90, 91, PD

[a]Notation used for key parameters:

n_{ed}	Electron density		Γ_{od}	Neutral hydrogen influxes
n_{od}	Neutral deuterium density		Γ_d^0	Impurity influxes (neutrals)
n_{zd}	Impurity ion density		v_z	Impurity streaming velocity
n_{id}	Deuteron density		v_0	Neutral deuterium streaming velocity
T_{ed}	Electron temperature		R_{sp}	Separatrix strike point
T_{zd}	Impurity temperature		Φ_0	Photon flux of neutral hydrogen line, W/(cm^2 ·nm·sr)
T_{id}	Deuteron temperature		Φ_z	Photon flux of impurity line, W/(cm^2 ·nm·sr)
T_{targ}	Target surface temperature		Γ_z	Gas fueling influx
P_{rad}	Total power radiated		Γ_1	Hydrogen influx in SOL (from n_i and v_i)

27

Table 4. He input/exhaust capability

Machine	Input	Exhaust	Date available
JET	^{3}He, ^{4}He (120, 140 keV; 7 A)	Wall pumping	Now
		Active pumping	1994
JT-60 U	^{3}He, ^{4}He (~80 keV, 3–5 MW)	Wall pumping	Now
		Active pumping	Planned
TFTR	He NBI, rf power (^{3}He)	Conditioned C-C tiles	Now
TEXT	None	None	—
ASDEX-U	40 keV, 300 mA		Plans
		Turbomolecular pumping (40,000 L/s He)	Now
DIII-D	He NBI (40–80 keV, to 1.8 MW/source, up to 8 sources)		Now
		Ar frost of ADP cryopump	Study
TEXTOR	He NBI (55 keV)		Now
		Turbomolecular pumping (S_{eff} = 4500 L/s)	Now

Table 5. Near-term and long-term issues

Machine	Near-term issues (6 months)	Longer-term issues
JET	(No distinction between near term and longer term)	
	Sawtooth effects, H/L-mode behavior, He in D plasma, D in He plasma, separation of recycle and central fueling, frictional transport effects, ICH power dependence, co-/counter-NBI, C or Be strike zone, pumping	
JT-60U	He transport/exhaust in H-mode plasma	He transport/exhaust in H/L-mode
	He ash control by ELMs	Parameter dependence (n_e, I_p, B_T, P_{heat})
		MeV alpha simulation ($D-^3He$ discharge)
		Ash control techniques: – ELM – sawtooth – ICRF – ergodic magnetic limiter
		Parameter scaling of τ_{He}
TFTR	Shut down until September 1991	Preparation for DT operation: – alpha-particle CHERS – gyrotron scattering – impurity pellets – limiter H-modes – rf tail alpha simulation
TEXT	Edge transport ($0.7 < r/a < 1.0$)	
ASDEX-U	Starting operation	Alpha source simulation by fusion products
		Bulk and boundary transport in L-mode and H-mode
DIII-D	CER calibration	(Not detailed → general plan)
	He NBI possible	He NBI (long pulse and modulated), with CER, divertor spectrometer, baffle partial pressure
		He pumping, if Ar frost is adopted
TEXTOR	He control techniques, He retention in walls, He transport studies with active exhaust	He self-pumping, He transport with improved spatial resolution, He transport under OH, L-mode, and enhanced confinement conditions

ORNL/TM-11935
Dist. Category UC-420

INTERNAL DISTRIBUTION

1.	Director, ORNL Fusion Energy Division	22–26.	J. T. Hogan
		27–31.	D. L. Hillis
2.	C. C. Baker	32.	D. B. Batchelor
3.	M. J. Saltmarsh	33.	C. A. Foster
4.	L. A Berry	34.	M. J. Gouge
5.	B. A. Carreras	35.	S. P. Hirshman
6.	R. A. Dory	36.	W. A. Houlberg
7.	J. L. Dunlap	37.	E. F. Jaeger
8.	H. H. Haselton	38.	C. C. Klepper
9.	M. S. Lubell	39.	R. A. Langley
10.	T. E. Shannon	40.	J. F. Lyon
11.	R. P. Leinius	41.	M. M. Menon
12–13.	Laboratory Records Department	42.	S. L. Milora
14.	Laboratory Records, ORNL-RC	43.	P. K. Mioduszewski
15–16.	Central Research Library	44.	G. H. Neilson
17.	Document Reference Section	45.	L. W. Owen
18.	Fusion Energy Division Library	46.	Y-K. M. Peng
		47.	C. C. Tsai
19–20.	Engineering Technology/Fusion Energy Division Publications Office	48.	N. A. Uckan
		49.	T. Uckan
21.	ORNL Patent Office	50.	J. J. Zielinski

EXTERNAL DISTRIBUTION

51. Office of the Assistant Manager for Energy Research and Development, U.S. Department of Energy Field Office, Oak Ridge, P.O. Box 2000, Oak Ridge, TN 37831
52. N. A. Davies, Director, Office of Fusion Energy, Office of Energy Research, ER-50 Germantown, U.S. Department of Energy, Washington, DC 20545
53. M. Roberts, International Programs, Office of Fusion Energy, Office of Energy Research, ER-52 Germantown, U.S. Department of Energy, Washington, DC 20545
54. D. E. Baldwin, L-640, Lawrence Livermore National Laboratory, P.O. Box 5511, Livermore, CA 94550
55. R. W. Conn, Mechanical, Aerospace, and Nuclear Engineering Department, 6291 Boelter Hall, University of California, Los Angeles, CA 90024-1597
56. R. Parker, Plasma Fusion Center, Massachusetts Institute of Technology, 167 Albany St., NW16-288, Cambridge, MA 02139
57. K. I. Thomassen, L-637, Lawrence Livermore National Laboratory, P.O. Box 5511, Livermore, CA 94550

58. J. D. Callen, Department of Nuclear Engineering, University of Wisconsin, Madison, WI 53706-1687

59. S. O. Dean, Fusion Power Associates, Inc., 2 Professional Drive, Suite 248, Gaithersburg, MD 20879

60. H. K. Forsen, Bechtel Group, Inc., Research Engineering, P.O. Box 3965, San Francisco, CA 94119

61. R. W. Gould, Department of Applied Physics, California Institute of Technology, Pasadena, CA 91125

62. R. A. Gross, Plasma Research Laboratory, Columbia University, New York, NY 10027

63. R. J. Hawryluk, Princeton Plasma Physics Laboratory, P.O. Box 451, Princeton, NJ 08543

64. P. C. Liewer, MS 138-208, Jet Propulsion Laboratory, 4800 Oak Grove Drive, Pasadena, CA 91109

65. D. M. Meade, Princeton Plasma Physics Laboratory, P.O. Box 451, Princeton, NJ 08543

66. W. M. Stacey, School of Nuclear Engineering and Health Physics, Georgia Institute of Technology, Atlanta, GA 30332

67. D. Steiner, Nuclear Engineering Department, NES Building, Tibbetts Avenue, Rensselaer Polytechnic Institute, Troy, NY 12181

68. R. Varma, Physical Research Laboratory, Navrangpura, Ahmedabad 380009, India

69. Bibliothek, Max-Planck Institut für Plasmaphysik, Boltzmannstrasse 2, D-8046 Garching, Federal Republic of Germany

70. Bibliothek, Institut für Plasmaphysik, KFA Jülich GmbH, Postfach 1913, D-5170 Jülich, Federal Republic of Germany

71. Bibliothek, KfK Karlsruhe GmbH, Postfach 3640, D-7500 Karlsruhe 1, Federal Republic of Germany

72. Bibliotheque, Centre de Recherches en Physique des Plasmas, Ecole Polytechnique Fédérale de Lausanne, 21 Avenue des Bains, CH-1007 Lausanne, Switzerland

73. R. Aymar, CEN/Cadarache, Departement de Recherches sur la Fusion Conrrôlée, F-13108 Saint-Paul-lez-Durance Cedex, France

74. Bibliothèque, CEN/Cadarache, F-13108 Saint-Paul-lez-Durance Cedex, France

75. Library, JET Joint Undertaking, Abingdon, Oxfordshire OX14 3EA, England

76. Library, FOM-Instituut voor Plasmafysica, Rijnhuizen, Edisonbaan 14, 3439 MN Nieuwegein, The Netherlands

77. Library, National Institute for Fusion Science, Chikusa-ku, Nagoya 464-01, Japan

78. Library, International Centre for Theoretical Physics, P.O. Box 586, I-34100 Trieste, Italy

79. Library, Centro Richerche Energia Frascati, C.P. 65, I-00044 Frascati (Roma), Italy

80. Library, Plasma Physics Laboratory, Kyoto University, Gokasho, Uji, Kyoto 611, Japan

81. Plasma Research Laboratory, Australian National University, P.O. Box 4, Canberra, A.C.T. 2601, Australia

82. Library, Japan Atomic Energy Research Institute, Naka Fusion Research Establishment, 801-1 Mukoyama, Naka-machi, Naka-gun, Ibaraki-ken, Japan

83. G. A. Eliseev, I. V. Kurchatov Institute of Atomic Energy, P.O. Box 3402, 123182 Moscow, U.S.S.R.

84. V. A. Glukhikh, Scientific-Research Institute of Electro-Physical Apparatus, 188631 Leningrad, U.S.S.R.

85. I. Shpigel, Institute of General Physics, U.S.S.R. Academy of Sciences, Ulitsa Vavilova 38, Moscow, U.S.S.R.

86. D. D. Ryutov, Institute of Nuclear Physics, Siberian Branch of the Academy of Sciences of the U.S.S.R., Sovetskaya St. 5, 630090 Novosibirsk, U.S.S.R.

87. O. Pavlichenko, Kharkov Physical-Technical Institute, Academical St. 1, 310108 Kharkov, U.S.S.R.

88. Deputy Director, Southwestern Institute of Physics, P.O. Box 15, Leshan, Sichuan, China (PRC)

89. Director, The Institute of Plasma Physics, P.O. Box 26, Hefei, Anhui, China (PRC)

90. D. H. Crandall, Division of Applied Plasma Physics, Office of Energy Research, ER-542, Germantown, U.S. Department of Energy, Washington, DC 20545

91. D. Markevich, Division of Applied Plasma Physics, Office of Energy Research, ER-542, Germantown, U.S. Department of Energy, Washington, DC 20545

92. R. H. McKnight, Experimental Plasma Physics Research Branch, Division of Applied Plasma Physics, Office of Energy Research, ER-542, Germantown, U.S. Department of Energy, Washington, DC 20545

93. E. Oktay, Division of Confinement Systems, Office of Energy Research, ER-55, Germantown, U.S. Department of Energy, Washington, DC 20545

94. W. L. Sadowski, Fusion Theory and Computer Services Branch, Division of Applied Plasma Physics, Office of Energy Research, ER-541, Germantown, U.S. Department of Energy, Washington, DC 20545

95. R. E. Mickens, Atlanta University, Department of Physics, Atlanta, GA 30314

96. M. N. Rosenbluth, University of California at San Diego, La Jolla, CA 92093

97. D. Schnack, SAIC, 10260 Campus Point Drive, San Diego, CA 92121

98. Duk-In Choi, Department of Physics, Korea Advanced Institute of Science and Technology, P.O. Box 150, Chong Ryang-Ri, Seoul, Korea

99. Library of Physics Department, University of Ioannina, Ioannina, Greece

100. C. De Palo, Library, Associazione EURATOM-ENEA sulla Fusione, CP 65, I-00044 Frascati (Roma), Italy

101. Theory Department Read File, c/o D. W. Ross, Institute for Fusion Studies, University of Texas, Austin, TX 78712

102. Theory Department Read File, c/o R. Parker, Director, Plasma Fusion Center, NW 16-202, Massachusetts Institute of Technology, Cambridge, MA 02139

103. Theory Department Read File, c/o R. White, Princeton Plasma Physics Laboratory, P.O. Box 451, Princeton, NJ 08543

104. Theory Department Read File, c/o L. Kovrizhnykh, Lebedev Institute of Physics, Academy of Sciences, 53 Leninsky Prospect, 117924 Moscow, U.S.S.R.

105. Theory Department Read File, c/o B. B. Kadomtsev, I. V. Kurchatov Institute of Atomic Energy, P.O. Box 3402, 123182 Moscow, U.S.S.R.

106. Theory Department Read File, c/o T. Kamimura, National Institute for Fusion Studies, Nagoya 464, Japan

107. Theory Department Read File, c/o E. Maschke, Departemente de Recherches sur la Fusion Controlée, CEN/Cadarache, F-13108 St.-Paul-lez-Durances, France

108. Theory Department Read File, c/o D. Düchs, JET Joint Undertaking, Abingdon, Oxfordshire OX14 3EA, United Kingdom

109. Theory Department Read File, c/o R. Briscoe, Culham Laboratory, Abingdon, Oxfordshire OX14 3DB, United Kingdom

110. Theory Department Read File, c/o D. Biskamp, Max-Planck-Institut fur Plasmaphysik, Boltzmannstrasse 2, D-8046 Garching, Federal Republic of Germany

111. Theory Department Read File, c/o T. Takeda, Japan Atomic Energy Research Institute, Tokai Fusion Research Establishment, Tokai-mura, Naka-gun, Ibaraki-ken, Japan

112. Theory Department Read File, c/o J. Greene, General Atomics, P.O. Box 85608, San Diego, CA 92186-9784

113. Theory Department Read File, c/o R. Cohen, Lawrence Livermore National Laboratory, P.O. Box 5511, Livermore, CA 94550

114. Theory Department Read File, c/o R. Gerwin, CTR Division, Los Alamos National Laboratory, P.O. Box 1663, Los Alamos, NM 87545

115. R. A. Blanken, Experimental Plasma Physics Research Branch, Division of Applied Plasma Physics, Office of Energy Research, ER-542, Germantown, U.S. Department of Energy, Washington, DC 20545

116. R. A. E. Bolton, IREQ Hydro-Quebec Research Institute, 1800 Montée-Ste.-Julie, Varennes, P.Q. JOL 2P0, Canada

117. R. L. Freeman, General Atomics, P. O. Box 85608, San Diego, CA 92186-9784

118. K. W. Gentle, RLM 11.222, Institute for Fusion Studies, University of Texas, Austin, TX 78712

119. R. J. Goldston, Princeton Plasma Physics Laboratory, P.O. Box 451, Princeton, NJ 08543

120. J. C. Hosea, Princeton Plasma Physics Laboratory, P.O. Box 451, Princeton, NJ 08543

121. J. W. Willis, Division of Confinement Systems, Office of Energy Research, ER-55, Germantown, U.S. Department of Energy, Washington, DC 20545

122. A. P. Navarro, Division de Fusion, CIEMAT, Avenida Complutense 22, E-28040 Madrid, Spain

123. Laboratory for Plasma and Fusion Studies, Department of Nuclear Engineering, Seoul National University, Shinrim-dong, Gwanak-ku, Seoul 151, Korea

124. D. Reiter, Institut für Plasmaphysik, KFA Jülich GmbH, Postfach 1913, D-5170 Jülich, Federal Republic of Germany

125. A. Nicolai, Institut für Plasmaphysik, KFA Jülich GmbH, Postfach 1913, D-5170 Jülich, Federal Republic of Germany

126. A. Pospieczszyk, Institut für Plasmaphysik, KFA Jülich GmbH, Postfach 1913, D-5170 Jülich, Federal Republic of Germany

127. D. Post, Princeton Plasma Physics Laboratory, P.O. Box 451, Princeton, NJ 08543

128. S. Cohen, Princeton Plasma Physics Laboratory, P.O. Box 451, Princeton, NJ 08543

129. J. Brooks, Bldg. 205, Argonne National Laboratory, 9700 S. Cass Avenue, Argonne, IL 60439

130. R. Gormley, Room 267, Plasma Fusion Center, Massachusetts Institute of Technology, 167 Albany Street, Cambridge, MA 02139

131. W. Rowan, RLM 12.216, Fusion Research Center, University of Texas, Austin, TX 78712

Princeton Plasma Physics Laboratory, P.O. Box 451, Princeton, NJ 08543

132. S. Jardin

133. M. Redi

134. N. Sauthoff   ,

135. E. Synakowski

Courant Institute of Mathematics and Sciences, New York University, 251 Mercer Street, New York, NY 10012

136. B. J. Braams

137. C. S. Chang

Fusion Studies Laboratory, Department of Nuclear Engineering, University of Illinois, 103 South Goodwin Avenue, Urbana, IL 61801

138. J. Guo

139. S. Hu

140. W. Hui

141. G. H. Miley

142. D. N. Ruzic

143. V. Varadarajan

General Atomics, P.O. Box 85608, San Diego, CA 92186-9784

144. A. Mahdavi

145. J. McChesney

146. R. Moyer

147. M. R. Wade

148. P. West

JAERI, Naka Fusion Research Establishment, Naka-Machi, Naka-Gun, Ibaraki-Ken 311-01, Japan

149. N. Fujisawa

150. H. Nakamura

151. Y. Shimomura

152. M. Sugihara

153. T. Tsunematsu

JET Joint Undertaking, Abingdon, OX14 3EA, Great Britain
- 154. M. A. von Hellerman
- 155. L. D. Horton
- 156. P. H. Rebut

Max-Planck-Institut für Plasmaphysik, Boltzmannstrasse 2, D-8046 Garching, Federal Republic of Germany
NET Team
- 157. K. Borrass
- 158. F. Engelmann
- 159. W. D. Haeseler
- 160. G. Pacher
- 161. H. Pacher

Experimentelle Plasmaphysik 1
- 162. H.-S. Bosch
- 162. U. Schumacher

Institut für Plasmaphysik, Forschungszentrum Jülich, IPP/KFA Jülich, P.O. Box 1913, Stetternicher Forst, D-5170 Jülich, Federal Republic of Germany
- 164. J. Boedo
- 165. K.-H. Dippel
- 166. H. Euringer
- 167. K.-H. Finken
- 168. J. Winter
- 169. G. Wolf

I. V. Kurchatov Institute of Atomic Energy, P.O. Box 3402, 123182 Moscow, U.S.S.R.
- 170. V. Abramov
- 171. S. Krasheninnikov
- 172. A. Kukushkin
- 173. S. Putvinskii

174–220. Given distribution as shown in OSTI-4500, Magnetic Fusion Energy (Category Distribution UC-420)